Delft University of Technology

First-Principles Study on the Elastic Mechanical Properties and Anisotropies of Gold–Copper Intermetallic Compounds

Wang, Jian; Qin, Hongbo; Chen, Junfu ; Yang, Daoguo; Zhang, Guoqi

Important note
To cite this publication, please use the final published version (if applicable).
Please check the document version above.

Article

First-Principles Study on the Elastic Mechanical Properties and Anisotropies of Gold–Copper Intermetallic Compounds

Jian Wang [1,2], **Hongbo Qin** [1,2,*], **Junfu Chen** [3,*], **Daoguo Yang** [1,2] and **Guoqi Zhang** [4]

1 Engineering Research Center of Electronic Information Materials and Devices, Ministry of Education, Guilin University of Electronic Technology, Guilin 541004, China; 20012201037@mails.guet.edu.cn (J.W.); d.g.yang@guet.edu.cn (D.Y.)

2 Guangxi Key Laboratory of Manufacturing System and Advanced Manufacturing Technology, School of Mechanical and Electrical Engineering, Guilin University of Electronic Technology, Guilin 541004, China

3 Guangdong Provincial Key Laboratory of Advanced Welding Technology, China-Ukraine Institute of Welding, Guangdong Academy of Sciences, Guangzhou 510650, China

4 EEMCS Faculty, Delft University of Technology, 2628 Delft, The Netherlands; g.q.zhang@tudelft.nl

* Correspondence: qinhb@guet.edu.cn (H.Q.); chenjf@gwi.gd.cn (J.C.); Tel.: +86-773-229-0108 (H.Q.)

Abstract: In this study, first-principles calculations were utilized to investigate the lattice constants, elastic constants, and mechanical properties of gold–copper (Au–Cu) intermetallic compounds (IMCs), including $AuCu_3$, $AuCu$, and Au_3Cu. We also verified the direction dependence of the Young's modulus, shear modulus, and Poisson's ratio of the compounds. The calculated lattice parameters agreed with the experimental data, and the single-crystal elastic constants, elastic modulus E, shear modulus G, bulk modulus B, and Poisson's ratio ν were calculated. For the Young's and shear moduli, $AuCu_3$ showed the highest anisotropy, followed by $AuCu$ and Au_3Cu. The Poisson's ratios of $AuCu_3$ and Au_3Cu crystals were isotropic on (100) and (111) crystal planes and anisotropic on the (110) crystal plane. However, the Poisson's ratio of the $AuCu$ crystal was anisotropic on (100) and (111) crystal planes and isotropic on the (110) crystal plane.

Keywords: first-principles; Au–Cu intermetallic compounds; mechanical properties; anisotropy

1. Introduction

Gold–copper (Au–Cu) alloy systems are binary mixtures with high electrical and thermal conductivities and excellent mechanical strength and chemical stability, and they are widely used in catalysis, electronics industries, and biological materials [1,2]. There are three Au–Cu intermetallic compounds (IMCs), including $AuCu_3$, $AuCu$, and Au_3Cu, in the Au–Cu alloy phase diagram reported by Okamoto et al. [3]. Janczak et al. [4] employed X-ray powder diffraction to study the composition and structure of Au–Cu IMCs during annealing and confirmed the presence of these three compounds. Ravi et al. [5] carried out mutual diffusion experiments of Au–Cu system at different temperatures. Singh et al. [6] examined the alloy behavior of Au–Cu via transmission electron microscopy and high-resolution phase-contrast microscopy. However, to date, the physical and mechanical properties of the three IMCs have not been determined due to the difficulty in obtaining pure samples of sufficient sizes. Several first-principles simulation studies on Au–Cu IMCs have been reported. Mohri et al. [7] conducted a complete phase stability analysis of Au–Cu IMCs. Xie et al. [8] calculated the potential energies, heat of formation, and critical temperatures of order–disorder transitions of $AuCu_3$, $AuCu$, and Au_3Cu IMCs and $AuCu_3$-, $AuCu$-, and Au_3Cu-type ordered alloys with maximal ordering degrees. Ozolins et al. [9] investigated the phase stability, thermodynamic properties, and bond lengths of Au–Cu alloys. Hu et al. [10] studied the stability and thermal properties of $AuCu_3$, $AuCu$, and Au_3Cu and calculated the phonon spectrum and phonon density of states. Kong et al. [11] evaluated the structure, elasticity, and thermodynamic properties of $AuCu_3$, $AuCu$, and Au_3Cu.

Although several studies on Au–Cu IMCs have been reported, most of them do not consider the anisotropy of Au–Cu IMCs. However, the abnormal growth of crystal grains, transformation and formation of material structure, and formation of microcracks are closely related to the anisotropy of the material [12,13]. There is, therefore, a need for further research on the elastic mechanical properties and anisotropy to increase the applications of Au–Cu IMC and improve the reliability and structure of designs. In this study, we calculated the elastic constants of monocrystalline $AuCu_3$, $AuCu$, and Au_3Cu based on the first-principles method. Next, according to the Voigt–Reuss–Hill approximation, we obtained the Young's, bulk, and shear moduli and the Poisson's ratio of polycrystalline IMCs. Finally, we examined the directional dependence and anisotropic degree of IMCs.

2. Methods and Computational Details

All first-principles calculations for Au–Cu IMCs were performed using the Cambridge Serial Total Energy Package (CASTEP) code based on the density functional theory (DFT) [14]. The generalized gradient approximation (GGA) with the Perdew–Burke–Ernzerhof (PBE) functional [15] was selected to estimate the exchange-correlation energy for Au and Cu. The kinetic energy cutoff and self-consistent field tolerance for plane waves were set at 440 eV and 1.0×10^{-6} eV/atom, respectively [11]. For different Au–Cu alloy structures, different Monkhorst–Pack grids [16] were used to sample the Brillouin zone to produce different *k*-points in each structure. The *k*-point sampling in the first irreducible zones of $AuCu_3$, $AuCu$, and Au_3Cu was $8 \times 8 \times 8$, $9 \times 9 \times 7$, and $8 \times 8 \times 8$, respectively. All *k*-point settings were convergent with respect to total energy (see Appendix A). The Broyden–Fletcher–Goldfarb–Shannon (BFGS) algorithm [17] was used to optimize the space group and lattice constants of the Au–Cu IMCs. The convergence tolerance of energy and maximum force were set at 4.0×10^{-6} eV/atom and 0.01 eV/Å. The maximum displacement was set at 4.0×10^{-4} Å. Figure 1 shows the unit cells of the three Au–Cu IMCs considered herein.
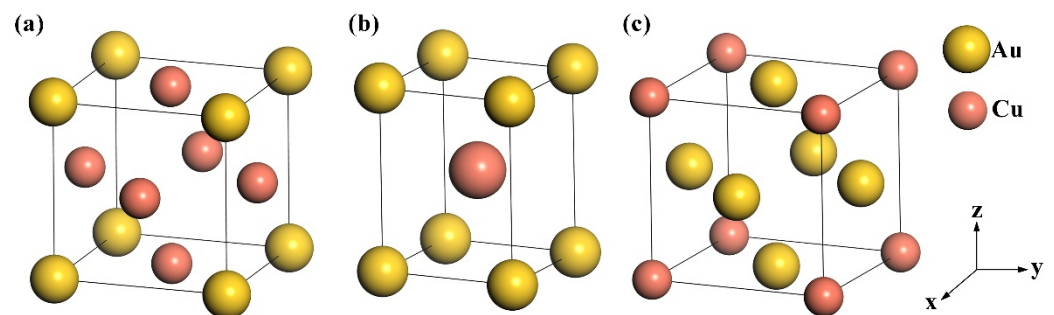
Figure 1. Crystal structures of gold–copper (Au–Cu) intermetallic compounds (IMCs): (**a**) $AuCu_3$, (**b**) $AuCu$, and (**c**) Au_3Cu.

3. Simulation Methods

3.1. Lattice Constants and Elastic Properties

$AuCu_3$, $AuCu$, and Au_3Cu were investigated, and Table 1 lists the calculated and experimental lattice constants. The calculated values are consistent with the experimental results with an average deviation of less than 2%.

Table 1. Calculated and experimental lattice constants of Au–Cu IMCs.

Phase	Ref.	Crystal System	Space Group	k-Points Mesh	a(Å)	c(Å)
AuCu$_3$	This work	Cubic	*Pm-3m*	$8 \times 8 \times 8$	3.778589	
	Exp. [18]				3.747000	
	error/%				0.84	
AuCu	This work	Tetragonal	*P4/mmm*	$9 \times 9 \times 7$	2.840972	3.708597
	Exp. [19]				2.806000	3.67000
	error/%				1.25	1.05
Au$_3$Cu	This work	Cubic	*Pm-3m*	$8 \times 8 \times 8$	4.042688	
	Exp. [20]				3.965000	
	error/%				1.96	

Elastic constants are vital for crystals. They can correlate the microscopic properties of materials with macroscopic mechanical behaviors. Elastic constants can be calculated using Hooke's law based on the stress–strain relationship:

$$\sigma_{ij} = C_{ijkl}\varepsilon_{ij} \tag{1}$$

where C_{ijkl} represents the elastic constant, also known as the stiffness matrix. The stress–strain matrix can be written as follows:

$$
\begin{pmatrix} \sigma_1 \\ \sigma_2 \\ \sigma_3 \\ \tau_1 \\ \tau_2 \\ \tau_3 \end{pmatrix} =
\begin{pmatrix}
C_{11} & C_{12} & C_{13} & C_{14} & C_{15} & C_{16} \\
 & C_{22} & C_{23} & C_{24} & C_{25} & C_{26} \\
 & & C_{33} & C_{34} & C_{35} & C_{36} \\
 & & & C_{44} & C_{45} & C_{46} \\
 & Sym. & & & C_{55} & C_{56} \\
 & & & & & C_{66}
\end{pmatrix}
\begin{pmatrix} \varepsilon_1 \\ \varepsilon_2 \\ \varepsilon_3 \\ \gamma_1 \\ \gamma_2 \\ \gamma_3 \end{pmatrix}
\tag{2}
$$

where σ_i, τ_i, ε_i, and γ_i are the normal stress, shear stress, normal strain, and shear strain, respectively. The elastic constants of AuCu$_3$, AuCu, and Au$_3$Cu calculated herein and the reported values are listed in Table 2. The two sets of data are in good agreement. The elastic flexibility matrix was obtained by inverting the elastic stiffness matrix (i.e., $S_{ij} = [C_{ij}]^{-1}$). According to the symmetry of Au–Cu IMCs, to express the elastic flexibility matrix, there are three S_{ij} (i.e., S_{11}, S_{12}, and S_{44}) for AuCu$_3$ and Au$_3$Cu and six S_{ij} (i.e, S_{11}, S_{12}, S_{13}, S_{33}, S_{44}, and S_{66}) for AuCu. Herein, the calculated values of S_{11}, S_{12}, and S_{44} for AuCu$_3$ were 0.01430, −0.00597, and 0.015380, respectively, and those for Au$_3$Cu are 0.02075, −0.00921, and 0.05313, respectively. For AuCu, S_{11}, S_{12}, S_{13}, S_{33}, S_{44}, and S_{66} were 0.00693, −0.00007, −0.00510, 0.01392, 0.02170, and 0.03424, respectively.

Table 2. Calculated elastic constants of Au–Cu IMCs (GPa).

Ref.	Phase	C_{11}	C_{33}	C_{44}	C_{66}	C_{12}	C_{13}
This work	AuCu$_3$	173.9		65.0		124.6	
Ref. [10]	AuCu$_3$	180.9		65.1		119.3	
This work	AuCu	231.7	158.1	46.1	29.2	89.0	117.6
Ref. [11]	AuCu	229.8	159.6	45.8	33.3	90.0	118.4
This work	Au$_3$Cu	165.2		18.8		131.8	
Ref. [11]	Au$_3$Cu	165.4		23.9		128.7	

Before calculating the Young's, shear, and bulk moduli and the Poisson's ratio of a lattice, it is important to examine its mechanical stability. For the cubic crystals, AuCu$_3$ and Au$_3$Cu, the mechanical stability criteria are as follows [21]:

$$C_{11} - C_{12} > 0, \ C_{11} > 0, \ C_{44} > 0, \ C_{11} + 2C_{12} > 0 \tag{3}$$

For the tetragonal crystal AuCu, the criteria are [22]:

$$
\begin{aligned}
&C_{11} > 0,\ C_{33} > 0,\ C_{44} > 0,\ C_{66} > 0,\ C_{11} - C_{12} > 0, \\
&C_{11} + C_{33} - 2C_{13} > 0,\ 2C_{11} + C_{33} + 2C_{12} + 4C_{13} > 0
\end{aligned}
\tag{4}
$$

According to the elastic constants listed in Table 2, the lattices of AuCu$_3$, AuCu, and Au$_3$Cu are stable. Moreover, the Young's, shear, and bulk moduli and the Poisson's ratio play decisive roles in evaluating the mechanical properties of the materials. Herein, the Voigt–Reuss–Hill (VRH) method [23] was employed to approximate the elastic moduli. The calculation of the elastic moduli based on the VRH approximation depends on the type of crystal. For the cubic crystals AuCu$_3$ and Au$_3$Cu, the bulk moduli, B_V and B_R, and shear moduli, G_V and G_R, can be calculated using Equations (5)–(8), respectively [24]:

$$
B_V = \frac{1}{3}(C_{11} + 2C_{12})
\tag{5}
$$

$$
G_V = \frac{1}{5}(C_{11} - C_{12} + 3C_{44})
\tag{6}
$$

$$
B_R = \frac{1}{3S_{11} + 6S_{12}}
\tag{7}
$$

$$
G_R = \frac{15}{4S_{11} - 4S_{12} + 3S_{44}}
\tag{8}
$$

For the tetragonal crystal AuCu, B_V, B_R, G_V, and G_R can be calculated using Equations (9)–(13), respectively [25]:

$$
B_V = \frac{1}{9}(2C_{11} + 2C_{12} + 4C_{13} + C_{33})
\tag{9}
$$

$$
B_R = \frac{C_{33}(C_{11} + C_{12}) - 2C_{13}^2}{C_{11} + C_{12} + 2C_{33} - 4C_{13}}
\tag{10}
$$

$$
G_V = \frac{1}{15}(2C_{11} - C_{12} - 2C_{13} + C_{33} + 6C_{44} + 2C_{66})
\tag{11}
$$

$$
G_R = \frac{15}{18B_V/C^2 + 6/(C_{11} - C_{12}) + 6/S_{44} + 3/C_{66}}
\tag{12}
$$

$$
C^2 = (C_{11} + C_{12})C_{33} - 2C_{13}^2
\tag{13}
$$

where B_V, B_R, G_V, and G_R are the upper and lower limits of the polycrystalline bulk modulus B and shear modulus G, respectively. The calculated bulk and shear moduli are the arithmetic average of the two limits [26]. The bulk modulus B and shear modulus G are expressed as follows:

$$
B = \frac{1}{2}(B_R + B_V)
\tag{14}
$$

$$
G = \frac{1}{2}(G_R + G_V)
\tag{15}
$$

Next, Young's modulus E and Poisson's ratio v can be calculated from B and G as Equations (16) and (17), respectively:

$$
E = \frac{9BG}{3B + G}
\tag{16}
$$

$$
v = \frac{3B - E}{6B}
\tag{17}
$$

The calculated B, G, E, and v are listed in Table 3. The bulk modulus reflects the resistance of a material to external uniform compression in an elastic system and is related to the elasticity of the chemical bond. Herein, the bulk moduli of the three IMCs were similar. The magnitude of the Young's modulus indicates the stiffness of the material. The

higher the Young's modulus of a material, the less likely it is to deform. Table 3 shows that the Young's modulus of Au–Cu IMCs decreased with increasing Au content (from AuCu$_3$ to Au$_3$Cu), and the shear modulus showed a similar trend. Poisson's ratio is an elastic constant that reflects the lateral deformation of a material. The calculated results show that Poisson's ratio increased with an increase in Au content in the three IMCs (Table 3). Vickers hardness H_V is calculated using Equation (18) [27]:

$$H_V = 0.92(G/B)^{1.3137}G^{0.708} \tag{18}$$

Table 3. Calculated bulk modulus B, shear modulus G, Young's modulus E, B/G ratio, Poisson ratio ν, and Vickers hardness H_V of Au–Cu IMCs.

Phase	B (GPa)			G (GPa)			B/G	E (GPa)	ν	H_V (GPa)
	B_V	B_R	B	G_V	G_R	G				
AuCu$_3$	141.03	141.03	141.03	48.88	39.31	44.09	3.20	119.80	0.358	2.919
AuCu	141.08	138.37	139.73	44.10	38.94	41.52	3.37	113.34	0.365	2.611
Au$_3$Cu	142.93	142.93	142.93	17.97	17.91	17.94	7.97	51.65	0.440	0.462

The calculated H_V is listed in Table 3. The Vickers hardness Hv and Young's modulus E of Au–Cu IMCs showed the same trend (i.e., AuCu$_3$ > AuCu > Au$_3$Cu). Pugh [28] established a ductility index (B/G ratio) to evaluate the ductility of materials. High values of B/G indicate high ductility, and vice versa. If the ratio is higher than 1.75, the material is ductile; otherwise, it is brittle. Herein, the B/G ratios of the three Au–Cu IMCs were higher than 1.75, implying that they are ductile materials. The ductility increased with the Au content. The Poisson's ratio ν is also related to B/G. A material with ν greater than 0.26 is considered ductile [29]. For the Au–Cu IMCs, B/G was greater than 1.75, and ν was greater than 0.26, confirming that they are ductile.

3.2. Elastic Anisotropy

Elastic anisotropy determines many basic properties of materials and is important for predicting the fracture toughness of materials. The universal anisotropy index A^U and percent anisotropy indices of compression and shear (A_B and A_G) are used to evaluate the elastic anisotropy of a material, and they are expressed as follows [11]:

$$A^U = 5\frac{G_V}{G_B} + \frac{B_V}{B_R} - 6 \tag{19}$$

$$A_B = \frac{B_V - B_R}{B_V + B_R} \times 100\% \tag{20}$$

$$A_G = \frac{G_V - G_R}{G_V + G_R} \times 100\% \tag{21}$$

For A^U, A_B, and A_G, if the value is 0, the crystal is isotropic. The greater their deviation from 0, the higher the degree of anisotropy. Herein, A^U of AuCu$_3$ was 1.217, indicating that AuCu$_3$ is anisotropic. The A_B and A_G were 0 and 10.85, respectively, indicating that AuCu$_3$ has no compression but shear anisotropy. The A^U, A_B, and A_G for AuCu were 0.682, 0.97, and 5.27, respectively, indicating that AuCu has lower universal, compression, and shear anisotropy. The A^U for Au$_3$Cu was 0.017, indicating that the degree of universal anisotropy of Au$_3$Cu is low. Also, the A_B and A_G for Au$_3$Cu were 0 and 0.17, respectively, indicating that the compound has no compressive anisotropy and weakest shear anisotropy.

To further investigate the tangential anisotropy of Au–Cu IMCs, we employed the anisotropy factors A_1, A_2, and A_3. The index of A_1 represented the shear anisotropy factor between [011] and [010] crystal orientations on the (100) crystal plane, Similarly, A_2 was the shear anisotropy factor between [101] and [001] orientations on the (010) crystal plane,

and A_3 was that between [110] and [010] orientations on the (001) crystal plane. For cubic crystals, A_1, A_2, and A_3 were expressed as follows [11]:

$$A_1 = A_2 = A_3 = \frac{4C_{44}}{C_{22} + C_{33} - 2C_{13}} \tag{22}$$

For tetragonal crystal [11]

$$A_1 = A_2 = \frac{4C_{44}}{C_{11} + C_{33} - 2C_{13}}, \; A_3 = \frac{4C_{66}}{2C_{11} - 2C_{12}} \tag{23}$$

The greater the difference between the anisotropy factors and 1, the higher the anisotropy of the crystal was. The calculated values are shown in Table 4. The A_1, A_2, and A_3 for $AuCu_3$ were 2.63, which is the highest deviation from 1, indicating that $AuCu_3$ exhibits the highest shear anisotropy. For Au_3Cu, the A_1, A_2, and A_3 were 1.13, indicating negligible shear anisotropy. For AuCu, the A_1 and A_2 were 1.19, and A_3 was 0.41, indicating that AuCu has mild shear anisotropy, between that of $AuCu_3$ and Au_3Cu.

Table 4. Calculated anisotropic index of Au–Cu IMCs.

Phase	$A^{\mathbf{U}}$	$A_{\mathbf{B}}$	$A_{\mathbf{G}}$	A_1	A_2	A_3
$AuCu_3$	1.217	0	10.85	2.63	2.63	2.63
AuCu	0.682	0.97	5.27	1.19	1.19	0.41
Au_3Cu	0.017	0	0.17	1.13	1.13	1.13

To further evaluate the anisotropy of Au–Cu IMCs, the Young's modulus in three dimensions was calculated. For the cubic crystals $AuCu_3$ and Au_3Cu, the three-dimensional (3D) expression of E is given by Equation (24) [24]:

$$\frac{1}{E} = S_{11} - 2(S_{11} - S_{12} - 0.5S_{44})\left(l_1^2 l_2^2 + l_2^2 l_3^2 + l_1^2 l_3^2\right) \tag{24}$$

For the tetragonal crystal, AuCu [30]

$$\frac{1}{E} = S_{11}\left(l_1^4 + l_2^4\right) + (2S_{13} + S_{44})\left(l_1^2 l_3^2 + l_2^2 l_3^2\right) + S_{33}l_3^4 + (2S_{12} + S_{66})l_1^2 l_2^2 \tag{25}$$

where l_1, l_2, and l_3 are the direction cosines of the a-, b-, and c-axes, respectively. Figures 2 and 3 show E for the 3D surface and cross-section of the IMCs. The degree of anisotropy depends on the deviation of a geometrical body from the spherical shape. If a geometrical body is a sphere, it exhibits isotropy. Thus, the Young's modulus of $AuCu_3$ showed the highest anisotropy, and that of Au_3Cu showed the lowest anisotropy, as shown in Figure 2. The Young's modulus of $AuCu_3$ had a maximum value of 169.05 GPa in the <111> crystal directions and a minimum value of 69.94 GPa in the <100> directions. In comparison, Au_3Cu had a maximum Young's modulus of 54.099 GPa in the <111> crystal orientation directions and a lowest Young's modulus of 48.19 GPa in the <100> crystallographic directions. The tetragonal AuCu had a maximum Young's modulus of 147.25 GPa in the [201], [021], [$\bar{2}$01], [0$\bar{2}$1], [$\bar{2}$0$\bar{1}$], [0$\bar{2}$$\bar{1}$], [20$\bar{1}$], and [02$\bar{1}$] directions and a minimum Young's modulus of 71.85 GPa in the [001] and [00$\bar{}$] directions. In directions perpendicular to the normal direction to the (001) plane, the bulk modulus had a maximum value of 568.86 GPa, whereas it was minimum in the [001] and [00$\bar{1}$] crystal directions (269.50 GPa). The maximum and minimum Young's moduli are listed in Table 5. The anisotropy ratio $E_{\max}/E_{\min}$ was employed to quantify the degree of anisotropy of the Young's modulus, and the larger the anisotropy ratio, the higher the anisotropy was [31]. $AuCu_3$ had the highest $E_{\max}/E_{\min}$ of 2.42, and Au_3Cu had the minimum value of 1.12.
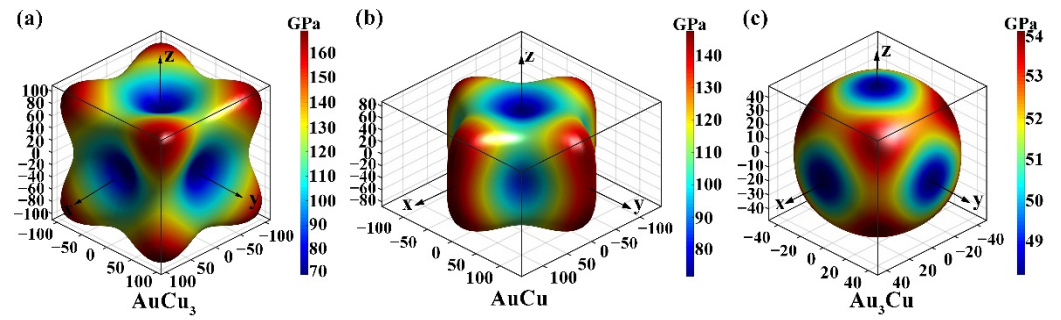
Figure 2. Directional dependence of Young's moduli: (**a**) Young's modulus of AuCu$_3$; (**b**) Young's modulus of AuCu; (**c**) Young's modulus of Au$_3$Cu.
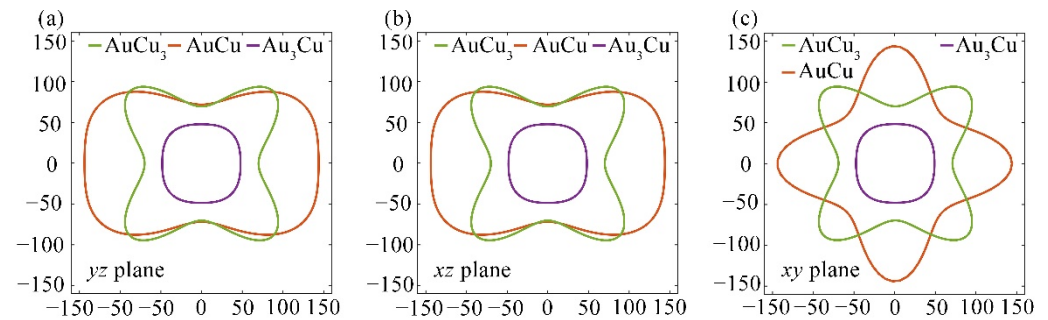

Figure 3. Cross-sections of Young's modulus E on the (**a**) yz, (**b**) xz, and (**c**) xy planes of AuCu$_3$, AuCu, and Au$_3$Cu.

Table 5. Anisotropy ratios and maximum and minimum Young's moduli E for AuCu$_3$, AuCu, and Au$_3$Cu.

	AuCu$_3$				AuCu				Au$_3$Cu			
	Whole	yz	xz	xy	**Whole**	yz	xz	xy	**Whole**	yz	xz	xy
$E_{\max}$ (GPa)	169.05	124.86	124.86	124.86	147.25	143.82	143.82	144.2	54.09	52.48	52.48	52.48
$E_{\min}$ (GPa)	69.94	69.94	69.94	69.94	71.85	71.85	71.85	83.41	48.19	48.19	48.19	48.19
Anisotropy ratios	2.42	1.79	1.79	1.79	2.05	2.00	2.00	1.73	1.12	1.09	1.09	1.09

Shear modulus G is related to $\boldsymbol{l}$ and $\boldsymbol{n}$, which are mutually perpendicular vectors (Figure 4). A crystal shears at the plane perpendicular to the vector $\boldsymbol{n}$. In a particular direction $\boldsymbol{l}$, G changes with $\boldsymbol{n}$, and it can be determined using Equation (26) [32].

$$
\begin{aligned}
\frac{1}{G}(\boldsymbol{l},\boldsymbol{n}) =\ & 4[2S_{12} - (S_{11} + S_{22} - S_{66})]l_1 n_1 l_2 n_2 + S_{66}(l_1 n_2 - l_2 n_1)^2 \\
& + 4(l_1 n_2 + l_2 n_1)[(S_{16} - S_{36})l_1 n_1 + (S_{26} - S_{36})l_2 n_2] + 4[2S_{23} - (S_{22} + S_{33} - S_{44})]l_2 n_2 l_3 n_3 \\
& + 4(l_2 n_3 + l_3 n_2)[(S_{24} - S_{14})l_2 n_2 + (S_{34} - S_{14})l_3 n_3] + 4[2S_{31} - (S_{33} + S_{11} - S_{55})]l_3 n_3 l_1 n_1 \\
& + 4(l_3 n_1 + l_1 n_3)[(S_{35} - S_{25})l_2 n_3 + (S_{15} - S_{25})l_1 n_1] + S_{44}(l_2 n_3 - l_3 n_2)^2 + S_{55}(l_3 n_1 - l_1 n_3)^2 \\
& + 2S_{45}(l_2 n_3 + l_3 n_2)(l_3 n_1 + l_1 n_3) + 2S_{56}(l_3 n_1 + l_1 n_3)(l_1 n_2 + l_2 n_1) + 2S_{64}(l_1 n_2 + l_2 n_1)(l_2 n_3 + l_3 n_2)
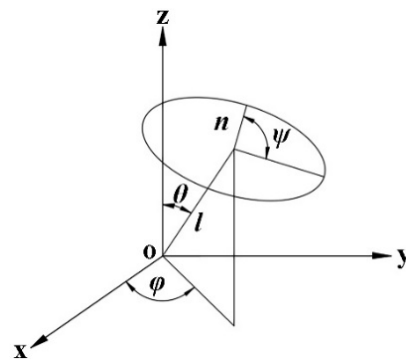\end{aligned}
\tag{26}
$$

Figure 4. Spherical coordinate diagrams of shear moduli *G* with respect to perpendicular vectors, *l* and *n*.

l and *n* are related as follows:

$$n_1 l_1 + n_2 l_2 + n_3 l_3 = 0 \tag{27}$$

Usually, the maximum and minimum values in each direction are used to evaluate the shear modulus *G*. Figures 5 and 6 show the 3D shape and cross-section of the shear modulus for the three Au–Cu IMCs. The shear anisotropy of $AuCu_3$ was the highest, followed by that of AuCu and Au_3Cu, which was consistent with A_G in Table 4. Furthermore, the maximum shear modulus of $AuCu_3$ was maximum in directions perpendicular to the (001), (010), and (100) crystal planes and minimum in the <111> direction. On the other hand, the minimum shear modulus was maximum in the <110> direction and maximum in the <100> direction. Similar to $AuCu_3$, the maximum shear modulus of Au_3Cu was minimum in <111> and maximum in directions perpendicular to the (001), (010), and (100) crystal planes. Additionally, the minimum shear modulus of Au_3Cu was maximum in the <100> direction and minimum in the <110> direction. As shown in Figure 5, the maximum shear modulus of AuCu was maximum in the [110], [$\bar{1}$10], [$\bar{1}\bar{1}$0], and [1$\bar{1}$0] crystal directions and minimum in the [011], [$\bar{1}$01], [0$\bar{1}$1], [101], [0$\bar{1}\bar{1}$], [10$\bar{1}$], [01$\bar{1}$], and [$\bar{1}$0$\bar{1}$] directions. On the other hand, the minimum shear modulus of AuCu was maximum in the [110], [$\bar{1}$10], [$\bar{1}\bar{1}$0], [1$\bar{1}$0], [001], and [00$\bar{1}$] directions and minimum in the <111> and [100], [$\bar{1}$00], [0$\bar{1}$0], and [010] crystal directions. The maximum and minimum values of the shear modulus *G* and the anisotropy ratio G_{max}/G_{min} for the compounds are listed in Table 6. $AuCu_3$ had the largest anisotropy ratio (2.63), and Au_3Cu had the lowest (1.13). For AuCu, the anisotropy ratio was 2.58 in all planes, and the anisotropy ratios of the *yz* and *xz* planes were the same (1.58), whereas that on the *xy* plane was 2.44.

Table 6. Anisotropy ratios and maximum and minimum share moduli *G* for $AuCu_3$, AuCu, and Au_3Cu.

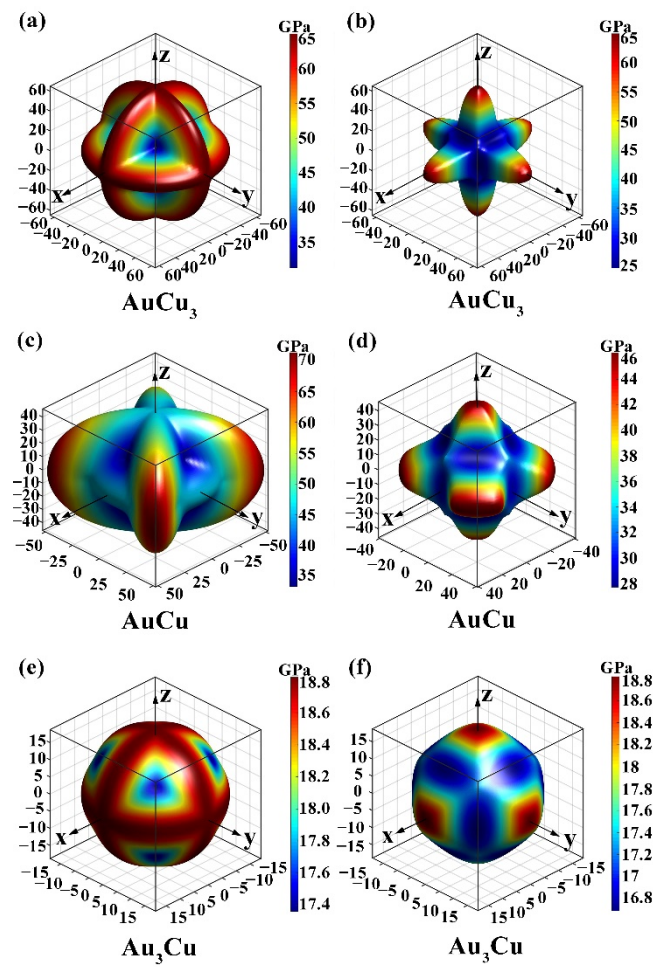|	$AuCu_3$				AuCu				Au_3Cu			
	Whole	*yz*	*xz*	*xy*	**Whole**	*yz*	*xz*	*xy*	**Whole**	*yz*	*xz*	*xy*
G_{max} (GPa)	65.02	65.02	65.02	65.02	71.31	46.10	46.10	71.31	18.82	18.82	18.82	18.82
G_{min} (GPa)	24.68	24.68	24.68	24.68	27.69	29.24	29.24	29.24	16.69	16.69	16.69	16.69
Anisotropy ratios	2.63	2.63	2.63	2.63	2.58	1.58	1.58	2.44	1.13	1.13	1.13	1.13

Figure 5. Direction dependence of shear modulus: (**a**) maximum shear modulus of AuCu₃; (**b**) minimum shear modulus of AuCu₃; (**c**) maximum shear modulus of AuCu; (**d**) minimum shear modulus of AuCu; (**e**) maximum shear modulus of Au₃Cu; and (**f**) minimum shear modulus of Au₃Cu.
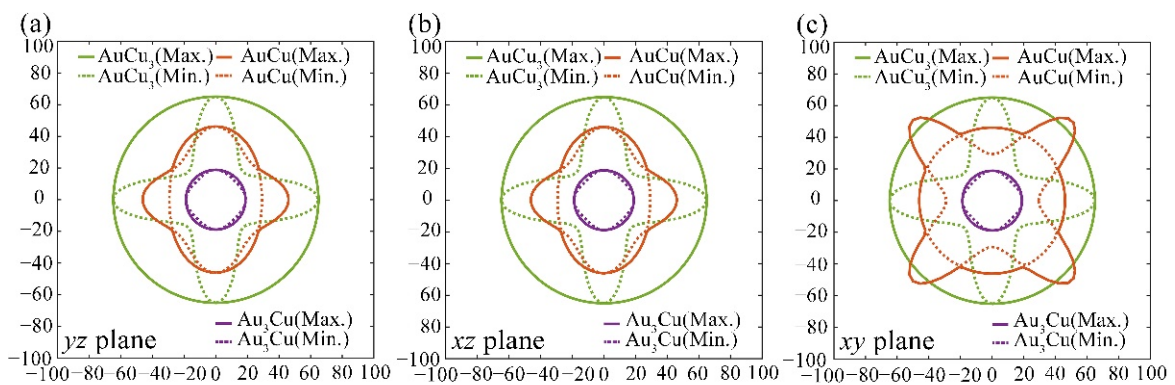

Figure 6. Cross-sections of shear modulus G in the (**a**) *yz*, (**b**) *xz*, and (**c**) *xy* planes for AuCu₃, AuCu, and Au₃Cu.

Poisson's ratio is an important index of elastic constant reflecting the transverse deformation of materials. For the cubic crystals $AuCu_3$ and Au_3Cu, the ratio is expressed as follows [33]:

$$v(hkl, \theta) = \left\{ S_{12} + \frac{S_0}{h^2+k^2+l^2} \left[\left(\frac{h^2 l}{\sqrt{h^2+k^2}\sqrt{h^2+k^2+l^2}} \cos\theta - \frac{hk}{\sqrt{h^2+k^2}} \sin\theta \right)^2 \right. \right.$$
$$\left. + \left(\frac{k^2 l}{\sqrt{h^2+k^2}\sqrt{h^2+k^2+l^2}} \cos\theta + \frac{hk}{\sqrt{h^2+k^2}} \sin\theta \right)^2 + \left(\frac{l\sqrt{h^2+k^2}}{\sqrt{h^2+k^2+l^2}} \cos\theta \right)^2 \right] \right\}$$
$$/ \left[-S_{11} + 2S_0 \frac{(hk)^2+(hl)^2+(lk)^2}{(h^2+k^2+l^2)^2} \right] \tag{28}$$

$$S_0 = S_{11} - S_{12} - \frac{1}{2}S_{44} \tag{29}$$

For the tetragonal crystal, AuCu [34]:

$$
\begin{aligned}
v(hkl, \theta) = -&\left\{ \frac{S_{11}}{h^2+k^2} \left[\left(\frac{h^2 L}{\sqrt{h^2+k^2+L^2}} \cos\theta - hk\sin\theta \right)^2 + \left(\frac{k^2 L}{\sqrt{h^2+k^2+L^2}} \cos\theta + hk\sin\theta \right)^2 \right] \right. \\
+&\frac{S_{12}}{h^2+k^2} \left[\left(\frac{hkl}{\sqrt{h^2+k^2+L^2}} \cos\theta - k^2\sin\theta \right)^2 + \left(\frac{hkL}{\sqrt{h^2+k^2+L^2}} \cos\theta + h^2\sin\theta \right)^2 \right] \\
&+ S_{13} \left[\left(h^2+k^2 \right) \cos^2\theta + L^2 \right] \\
+&\frac{S_{66}}{h^2+k^2} \left(\frac{hkl}{\sqrt{h^2+k^2+L^2}} \cos\theta - k^2\sin\theta \right) \left(\frac{hkL}{\sqrt{h^2+k^2+L^2}} \cos\theta + h^2\sin\theta \right) \\
+&\left(S_{33} - 2S_{13} - S_{44} \right) \frac{(h^2+k^2)L^2}{h^2+k^2+L^2} \cos^2\theta \right\} \\
\times &\frac{h^2+k^2+L^2}{S_{11}(h^4+k^4)+(2S_{12}+S_{66})h^2k^2+(2S_{13}+S_{44})(h^2+k^2)L^2+S_{33}L^4}
\end{aligned}
\tag{30}
$$

where *h*, *k*, and *l* are the Miller indices. $L = (a/c)l$, where *a* and *c* are the lattice constants of the tetragonal crystal. The Poisson's ratios of the three IMCs on three low-index crystal planes ((100), (110), and (111)) along different directions are shown in Figures 7–9. The Poisson's ratios of $AuCu_3$ on the (100) and (111) crystal planes were 0.417 and 0.300, respectively, and the shape was circular, indicating that it is isotropic. However, it showed high anisotropy on the (110) crystal plane, and the minimum and maximum values were 0.040 and 0.745 in [$\bar{1}$10] and [00$\bar{1}$] directions, respectively. For AuCu, the Poisson's ratio was circular on the (110) crystal plane with a value of 0.428, indicating no anisotropy. AuCu exhibited anisotropy on the (100) plane with Poisson's ratios of 0.019 and 0.736 for the [010] and [00$\bar{1}$] directions, respectively. AuCu also showed high anisotropy on the (111) plane with Poisson's ratios of 0.518 and 0.260 in [$\bar{1}$10] and [11$\bar{2}$] crystal directions, respectively. Further, the Poisson's ratio of Au_3Cu on (100) and (111) crystal planes was 0.444 and 0.437, respectively, indicating no significant anisotropy on the planes. However, it exhibited anisotropy on the (110) crystal plane, where the minimum and maximum values were 0.39 and 0.48 in the [$\bar{1}$10] and [00$\bar{1}$] directions, respectively. In summary, for Poisson's ratio, Au_3Cu and $AuCu_3$ crystals exhibited isotropy on the (100) and (111) crystal planes and anisotropy on the (110) crystal plane, whereas AuCu was anisotropic on the (100) and (111) crystal planes and isotropic on the (110) crystal plane.
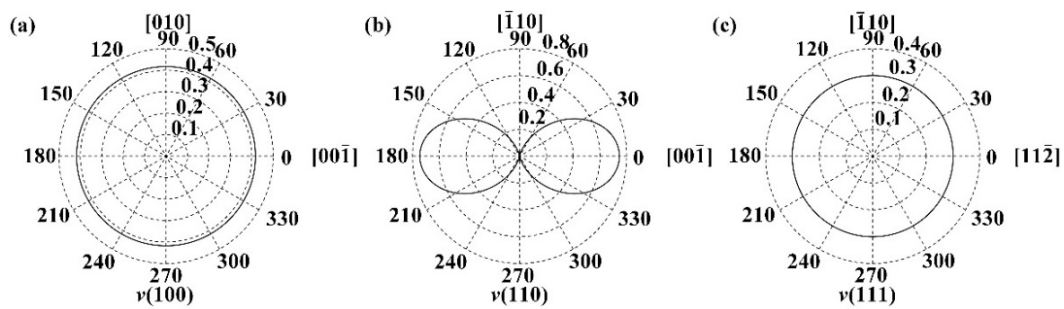
Figure 7. Direction dependence of Poisson's ratio on low-index planes of AuCu$_3$: (**a**) (100), (**b**) (110), and (**c**) (111).
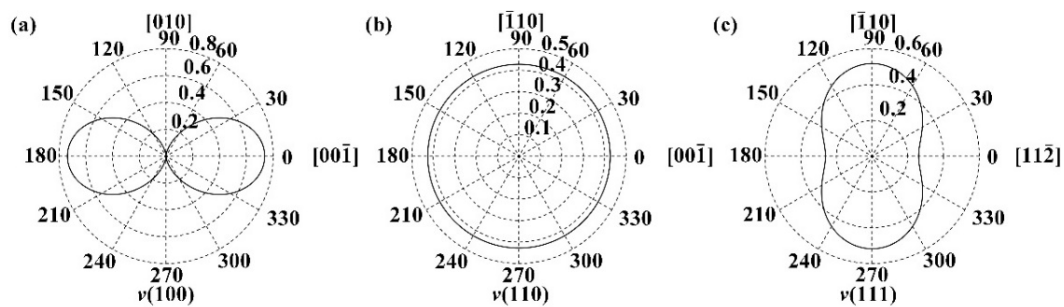

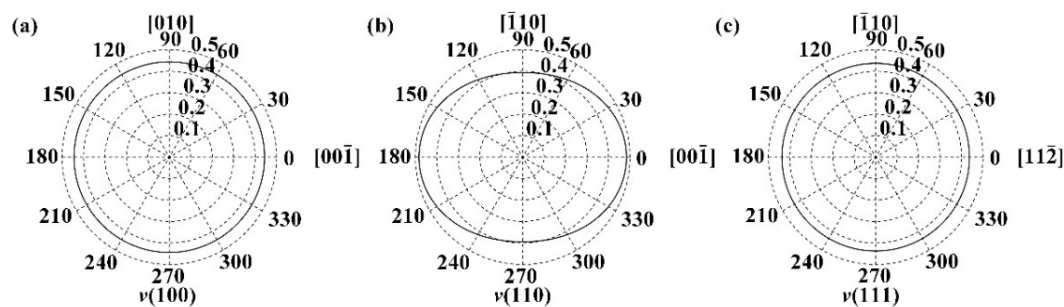**Figure 8.** Direction dependence of Poisson's ratio on low-index planes of AuCu: (**a**) (100), (**b**) (110), and (**c**) (111).

Figure 9. Direction dependence of Poisson's ratio on low-index planes of Au$_3$Cu: (**a**) (100), (**b**) (110), and (**c**) (111).

4. Conclusions

In this study, we employed the first-principles method to extensively explore the elastic mechanical properties and anisotropy of Au–Cu IMCs, and the following conclusions were drawn from the results:

1. The Young's modulus, shear modulus, and Poisson's ratio increased with Au content (i.e., from AuCu$_3$ through AuCu to Au$_3$Cu). However, the bulk moduli of the compounds were similar.
2. The Au–Cu IMCs exhibited excellent ductility in this order: Au$_3$Cu > AuCu > AuCu$_3$.
3. For the Young's modulus and shear modulus, the three Au–Cu IMCs were anisotropic, and among them, AuCu$_3$ showed the highest anisotropy.
4. The Poisson's ratios of Au$_3$Cu and AuCu$_3$ were isotropic on the (100) and (111) crystal planes and anisotropic on the (110) crystal plane. However, the Poisson's ratio of the AuCu crystal was anisotropic on the (100) and (111) crystal planes and isotropic on the (110) crystal plane.

Appendix A

The relationship between the *k*-point and total energy is presented in Figure A1. For $AuCu_3$, AuCu, and Au_3Cu, the total energies began to converge when the *k*-points increased to $3 \times 3 \times 3$, $3 \times 3 \times 2$, and $3 \times 3 \times 3$, respectively. The dependence between the *k*-point and elastic constants C_{ij} are shown in Figure A2. Similarly, the elastic constants of the three IMCs converged when the *k*-points rose to $3 \times 3 \times 3$, $3 \times 3 \times 2$, and $3 \times 3 \times 3$, respectively. Therefore, the *k*-points of $AuCu_3$, AuCu, and Au_3Cu ($8 \times 8 \times 8$, $9 \times 9 \times 7$, and $8 \times 8 \times 8$) were convergent with respect to the elastic constant C_{ij}.
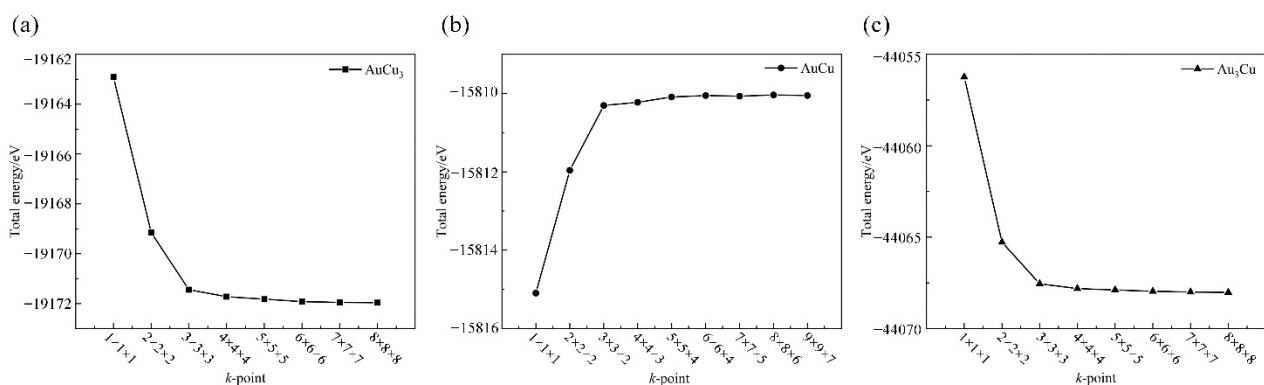

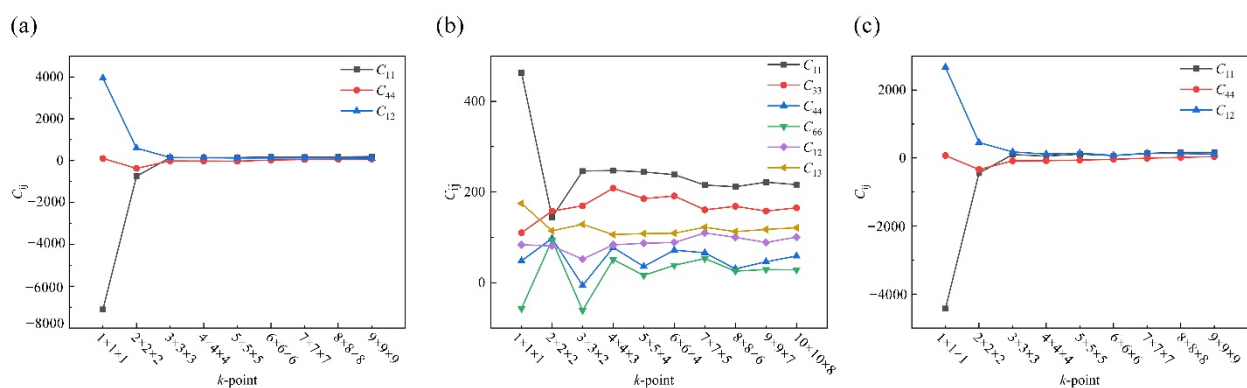**Figure A1.** The relationship between *k*-point and total energy: (**a**) $AuCu_3$, (**b**) AuCu, (**c**) Au_3Cu.

Figure A2. The relationship between *k*-point and elastic constants C_{ij}: (**a**) $AuCu_3$, (**b**) AuCu, (**c**) Au_3Cu.

References

1. Aish, M. Mechanical properties and sound velocity of gold copper (AuCu) II superlattice: 3D molecular dynamic (MD) simulation. *J. Theor. Appl. Mech.* **2020**, *58*, 901–909. [CrossRef]
2. Huang, Y.; Liu, W.; Ma, Y.; Tang, S.; Wang, J.; Chen, B. A novel interface strengthening layer: Nanoscale AuCu super-structure formed during Au80Sn20/Cu rapid solidification soldering process. *Mater. Charact.* **2017**, *135*, 214–220. [CrossRef]
3. Okamoto, H.; Chakrabarti, D.J.; Laughlin, D.E.; Massalski, T.B. The Au−Cu (Gold-Copper) system. *J. Phase Equilib.* **1987**, *8*, 454–474. [CrossRef]
4. Janczak, J.; Kubiak, R. X-Ray Study of Annealing Process of Au3Cu, AuCu and AuCu3 at 270 °C in Air. *Mater. Sci. Forum* **1991**, *79*, 567–574. [CrossRef]
5. Ravi, R.; Paul, A. Diffusion mechanism in the gold-copper system. *J. Mater. Sci.-Mater. Electron.* **2012**, *23*, 2152–2156. [CrossRef]
6. Singh, M.K.; Chettri, P.; Basu, J.; Tripathi, A.; Mukherjee, B.; Tiwari, A.; Mandal, R.K. Synthesis of anisotropic Au–Cu alloy nanostructures and its application in SERS for detection of methylene blue. *Mater. Res. Express.* **2020**, *7*, 015–052. [CrossRef]
7. Mohri, T.; Terakura, K.; Takizawa, S.; Sanchez, M.J. First-principles study of short range order and instabilities in AuCu, AuAg and AuPd alloys. *Acta Metall. Mater.* **1991**, *39*, 493–501. [CrossRef]
8. Xie, Y.Q.; Liu, X.B.; Li, X.B.; Peng, H.J.; Nie, Y.Z. Potential energies of characteristic atoms on basis of experimental heats of formation of AuCu and AuCu3 compounds (I). *Trans. Nonferrous Met. Soc. China* **2009**, *19*, 1243–1256. [CrossRef]
9. Ozolins, V.; Wolverton, C.; Zunger, A. Cu-Au, Ag-Au, Cu-Ag and Ni-Au intermetallics: First-principles study of phase diagrams and structures. *Phys. Rev. B Condens. Matter* **1997**, *57*, 6427–6443. [CrossRef]
10. Hu, J.; Xie, M.; Zhang, J.; Yang, Y.; Liu, M.; Chen, Y.; Chen, S.; Wang, S.; Wang, S. First Principles Study of Stability and Thermal Properties of AuxCuy Compounds. *Rare Metal Mater. Eng.* **2015**, *44*, 2677–2682.
11. Kong, G.X.; Ma, X.J.; Liu, Q.J.; Yong, L.; Liu, Z.T. Structural stability, elastic and thermodynamic properties of Au–Cu alloys from first-principles calculations. *Phys. B Condens. Matter* **2018**, *533*, 58–62. [CrossRef]
12. Zhang, J.M.; Zhang, Y.; Xu, K.W. Dependence of stresses and strain energies on grain orientations in FCC metal films. *J. Cryst. Growth* **2005**, *285*, 427–435. [CrossRef]
13. Choi, J.H.; Kang, S.Y.; Dong, N.L. Relationship between deposition and recrystallization textures of copper and chromium electrodeposits. *J. Mater. Sci.* **2000**, *35*, 4055–4066. [CrossRef]
14. Segall, M.D.; Lindan, P.J.D.; Probert, M.J.; Pickard, C.J.; Hasnip, P.J.; Clark, S.J.; Payne, M.C. First-principles simulation: Ideas, illustrations and the CASTEP code. *J. Phys. Condens. Matter* **2002**, *14*, 2717–2744. [CrossRef]
15. Perdew, J.P.; Burke, K.; Ernzerhof, M. Generalized Gradient Approximation Made Simple. *Phys. Rev. Lett.* **1998**, *77*, 3865–3868. [CrossRef]
16. Monkhorst, H.J.; Pack, J.D. Special points for Brillouin-zone integrations. *Phys. Rev. B Condens. Matter* **1976**, *13*, 5188–5192. [CrossRef]
17. Pfrommer, B.G.; Cote, M.; Louie, S.G. Relaxation of crystals with the quasi-Newton method. *J. Comput. Phys.* **1997**, *131*, 233–240. [CrossRef]
18. Kubiak, R.; Janczak, J. X-ray study of ordered phase formation in Au31.6Cu68.4, Au50Cu50 and Au75Cu25. *J. Alloys Compd.* **1991**, *176*, 133–140. [CrossRef]
19. Bjerkelund, E.; Pearson, W.B.; Selte, K.; Kjekshus, A.; Hagen, G. Lattice Parameters of the CuAu(I) Phase. *Acta Chem. Scand.* **1967**, *21*, 2900–2902. [CrossRef]
20. Flinn, P.A.; Mcmanus, G.M.; Rayne, J.A. Elastic constants of ordered and disordered Cu3Au from 4.2 to 300° K. *J. Phys. Chem. Solids* **1960**, *15*, 189–195. [CrossRef]
21. Nye, J.F. *Physical Properties of Crystals: Their Representation by Tensors and Matrices*; Oxford University Press: Oxford, UK, 1985.
22. Zhou, Y.X.; Yan, P.; Chong, X.Y.; Feng, J. Revealing the stability, elastic properties and electronic structures of Pd-V intermetallics via first principle calculations. *AIP Adv.* **2018**, *8*, 105132. [CrossRef]
23. Francis, G.P.; Payne, M.C. Finite basis set corrections to total energy pseudopotential calculations. *J. Phys. Condens. Matter* **1990**, *2*, 4395. [CrossRef]
24. Luan, X.; Qin, H.; Liu, F.; Dai, Z.; Yi, Y.; Li, Q. The mechanical properties and elastic anisotropies of cubic Ni3Al from first principles calculations. *Crystals* **2018**, *8*, 307. [CrossRef]
25. Wang, X.; Bao, L.; Wang, Y.; Wu, Y.; Duan, Y.; Peng, M. Explorations of electronic, elastic and thermal properties of tetragonal TM4N3 (TM= V, Nb and Ta) nitrides. *Mater. Today Commun.* **2021**, *26*, 101723. [CrossRef]
26. Hill, R. The elastic behaviour of a crystalline aggregate. *Proc. Phys. Soc. Lond. Sect. A.* **1952**, *65*, 349. [CrossRef]
27. Tian, Y.; Xu, B.; Zhao, Z. Microscopic theory of hardness and design of novel superhard crystals. *Int. J. Refract. Met. Hard Mater* **2012**, *33*, 93–106. [CrossRef]
28. Pugh, S.F. XCII. Relations between the elastic moduli and the plastic properties of polycrystalline pure metals. *Philos. Mag.* **1954**, *45*, 823–843. [CrossRef]
29. Zhang, X.; Jiang, W. First-principles investigation on the mechanical, vibrational and thermodynamics properties of AuCu3-type X3Sc (X= Al, Ga, In) intermetallic compounds. *Comput. Mater. Sci.* **2015**, *106*, 38–44. [CrossRef]
30. Li, R.-Y.; Duan, Y.-H. Anisotropic elastic properties of MB (M= Cr, Mo, W) monoborides: A first-principles investigation. *Philos. Mag.* **2016**, *96*, 972–990. [CrossRef]

31. Gomis, O.; Manjón, F.-J.; Rodríguez-Hernández, P.; Muñoz, A. Elastic and thermodynamic properties of α-Bi2O3 at high pressures: Study of mechanical and dynamical stability. *J. Phys. Chem. Solids* **2019**, *124*, 111–120. [CrossRef]

32. Ting, T.C.T. On Anisotropic Elastic Materials for which Young's Modulus E (n) is Independent of n or the Shear Modulus G (n, m) is Independent of n and m. *J. Elast.* **2005**, *81*, 271–292. [CrossRef]

33. Zhang, J.-M.; Zhang, Y.; Xu, K.-W.; Ji, V. Young's modulus surface and Poisson's ratio curve for cubic metals. *J. Phys. Chem. Solids* **2007**, *68*, 503–510. [CrossRef]

34. Zhang, J.-M.; Zhang, Y.; Xu, K.-W.; Ji, V. Young's modulus surface and Poisson's ratio curve for tetragonal crystals. *Chin. Phys. B* **2008**, *17*, 15–65.